Chemically Reacting Hypersonic Flows Over 3D Cavities: Flowfield Structure Characterisation

Rodrigo C. Palharini[1]

Instituto de Aeronáutica e Espaço, 12228-904 São José dos Campos, SP, Brazil

Thomas J. Scanlon[3]

Department of Mechanical & Aerospace Engineering, University of Strathclyde, Glasgow, G1 1XJ, UK

Craig White[2]

School of Engineering, University of Glasgow, Glasgow G12 8QQ, UK

Abstract

In this paper, a computational investigation of hypersonic rarefied gas flows in the transitional flow regime over 3D cavities is carried out by using the direct simulation Monte Carlo method. Such cavities give rise to geometric discontinuities that are often present at the surface of reentry vehicles. This work is focused on the flowfield structure characterisation under a rarefied environment and in the presence of chemical reactions. The cavities are investigated with different length-to-depth ratios, and the different flow structures are studied. In particular, for length-to-depth ratios of 1 and 2, a single recirculation is observed inside the cavities and the main flow is not able to enter the cavity due to the recirculation structure and high particle density. In the case of length-to-depth ratio 3, the flow is able to partially enter the cavity resulting in a elongated recirculation and the beginning of a secondary recirculation core is noticed. For the case of values 4 and 5, the main flow is able to penetrate deeper into the cavities and two recirculation zones are observed; however, for the length-to-depth

[1]Postdoctoral Research Fellow, Division of Aerodynamics.
[2]Senior Lecturer, James Weir Fluids Laboratory.
[3]Lecturer, University of Glasgow.

ratio 5 the flow impinges directly on the bottom surface, which is a behaviour that is only observed in the continuum regime with a cavity length-to-depth ratio greater than 14.

Keywords: Cavity flows, DSMC, Rarefied gas, Thermal protection system, Reentry.

1. Introduction

Space vehicles reentering the Earth's atmosphere may achieve speeds of tens of km/s. In order to slow down and reach landing speed, the spacecraft experiences atmospheric friction effects which produce external surface temperatures as high as 1700 K, well above the melting point of steel. Although such hypersonic vehicles are built with advanced materials and methods, the airframe is constructed using lightweight aluminum and can only withstand temperatures ranging from 750 to 900 K without annealing or softening. In this scenario, reliable heat shields are required to protect the vehicle's surface and its crew from the extremely hostile re-entry environment [1, 2].

External insulation materials such as Reinforced Carbon-Carbon (RCC), Low- and High-Temperature Reusable Surface Insulation tiles (LRSI and HRSI, respectively), and Felt Reusable Surface Insulation (FRSI) blankets have been developed for such applications [3]. These materials are bonded to a substrate, either directly to the airframe or to a supporting structure. For the Space Shuttle's development flights, more than 32,000 individual thermal protections system (TPS) tiles were used to cover the lower and upper surfaces. The tiles were arranged in a staggered or aligned pattern on the spacecraft surface and this can create numerous panel-to-panel joints. As such, cavities, gaps, and steps are often present on the surface of the aerospace vehicle. The implications for engineering and design requirements include the ability to account for thermal expansion and contraction of non-similar materials. In addition, gaps may be introduced by sensor installations, retro-propulsion systems, parachute and landing gears bays, or may be caused by the impact of orbiting debris or

near field experiments [4–7]. These discontinuities at the TPS can lead to the appearance of stagnation points, hot spots, flow separation and attachment or it may induce an early boundary layer transition from a laminar to turbulent conditions [8, 9].

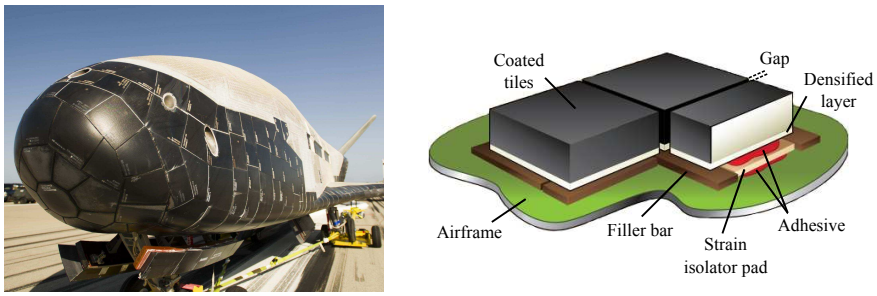

Figure 1: (a) X-37B space plane, (b) thermal protection system airframe (images credit: NASA).

Many experimental and numerical studies have been carried out to define and develop new materials for reusable thermal protections system that could withstand the harsh reentry environment and to accurately predict the required spacing between the TPS tiles [10–28]. Based on the available literature [19, 20, 24, 27, 29], high speed flows over cavities may be classified into four types. These four types, as shown in Fig. 2, appear to be primarily a function of the cavity length-to-depth ratio as briefly described below:

- Gap (L/D $<$ 1): The first flow type occurs for very short or deep cavities. The induced shearing provokes the main flow to develop a column of counter rotating vortices inside the gap and hot spots occur when the vortices directionally align and impinge on the sidewall.

- Open cavity (1 $<$ L/D $<$ 10): The mainstream flow does not enter the cavity directly and the high pressures ahead of the rear face and low pressure region downstream of the front face cause the shear layer to flow over or bridge the cavity. A weak shock wave may be formed near the

downstream lip as a result of the flow being compressed by the shear layer and heat fluxes slowly increase at this region. The pressure coefficients over the cavity floor are slightly positive and relatively uniform with a small adverse gradient occurring ahead of the rear face due the shear layer reattachment on the outer edge of this face.

- Transitional cavity ($10 < L/D < 14$): Typically characterised by unsteady flow behaviour since it alternates between an open and closed cavity. In this case, the shear layer turns through an angle to exit from the cavity coincident with the impingement shock and the exit shock collapsing into a single wave. A pressure plateau is observed in the reattachment region and a uniform pressure increase from the low values in the region aft of the front face with peak values on the rear face.

- Close cavity ($L/D > 14$): In this case, the shear layer separates from the upstream cavity lip, reattaches at some point on the cavity floor, and then separates again before reaching the cavity rear face. Two distinct separation regions are formed, one downstream of the forward face and one upstream of the rear face. The cavity floor pressure distribution consists of low pressures in the separation region followed by an increase in pressure and pressure plateau occurring in the reattachment region. The local flow over the cavity front and rear faces are very similar to the flows over reward-facing and forward-facing steps, respectively.

On the 1st of February 2003, the Space Shuttle Columbia experienced a catastrophic failure during atmospheric reentry at Mach 18 and an altitude of 61.3 km. According to th Columbia Accident Investigation Board (CAIB) and supported by the NASA Accident Investigation Team (NAIT), the most probable cause for the loss of the Space Shuttle Columbia was a breach in the thermal protection system of the leading edge of the left wing caused by a fragment of insulation foam released from external fuel tank during the ascent, exposing the wing structure to high energy air flow [30, 31].

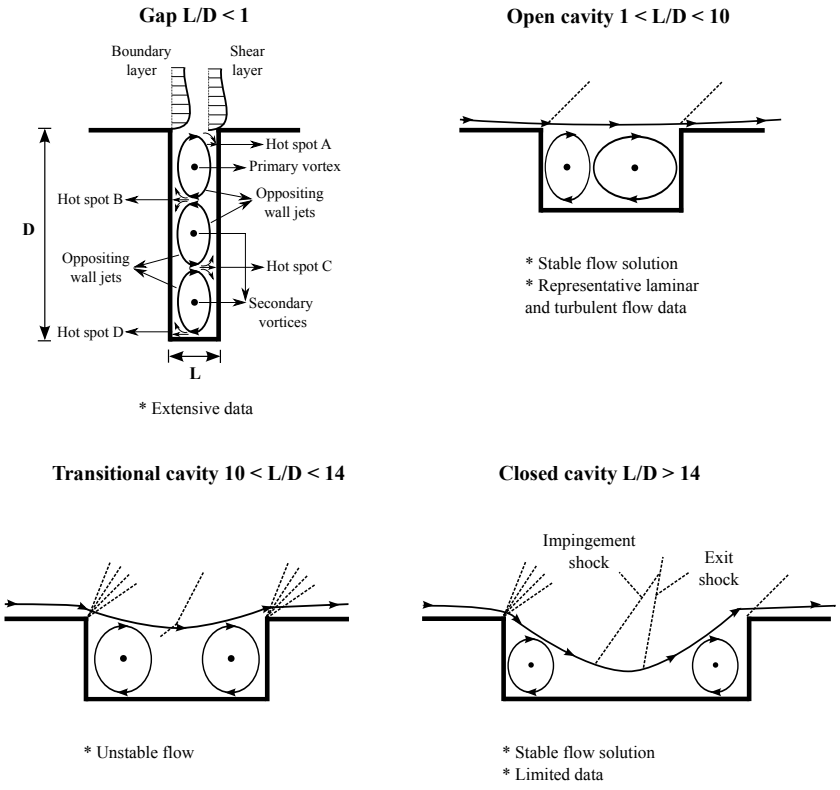

Figure 2: Cavity flowfield structure in the continuum regime [24].

The Space Shuttle accident highlights the complexity of the study of flow over TPS discontinuities under reentry conditions. Furthermore, it indicates that an accurate understanding of the flow structure inside cavities is a necessary requirement for an optimal design of re-entry vehicles. In the present work, reactive hypersonic gas flows over 3D cavities are investigated for different length-to-depth (L/D) ratios in the transitional flow regime in order to obtain a more profound understanding of the flow structure in such geometries under rarefied conditions. At this flow condition, the direct simulation Monte Carlo technique is the most appropriated computational method to be used.

2. The DSMC method

The direct simulation Monte Carlo method (DSMC) was almost exclusively developed by Bird [32] between 1960 and 1980 and has become one of the most important numerical techniques for solving rarefied gas flows in the transition regime. The DSMC method is based on physical concepts of rarefied gases and on the physical assumptions that form the basis for the derivation of the Boltzmann equation [33]. However, the DSMC method is not derived directly from the Boltzmann equation. As both the DSMC method and the Boltzmann equation are based on classical kinetic theory, then the DSMC method is subject to the same restrictions as the Boltzmann equation, i.e., assumption of molecular chaos and restrictions related to dilute gases.

The DSMC method models the flow as a collection of particles or molecules. Each particle has a position, velocity, and internal energies. The state of the particle is stored and modified with the time as the particles move, collide and interact with the surface in the simulated physical domain [34]. The assumption of dilute gas, where the mean molecular diameter is much smaller than the mean molecular space in the gas, allows the molecular motion to be decoupled from the molecular collisions. Particle movement is modelled deterministically, while collisions are treated statistically. Since it is impractical to simulate the real number of particles in the computational domain, a small number of representative particles are used and each one represents a large number of real atoms/molecules. Simulations can vary from thousands to millions of DSMC simulators particles in rarefied flow problems.

The linear dimensions of the cells should be small in comparison with the length of the macroscopic flow gradients normal to the streamwise directions, which means that the cell dimensions should be the order of or smaller than the local mean free path [32, 35, 36]. Another requirement of the DSMC method is the setting of an appropriate time step Δt. The trajectories of the particles in physical space are calculated under the assumption of the decoupling between the particle motion and the intermolecular collisions. The time step should

be chosen to be sufficiently small in comparison with the local mean collision time [37, 38].

When dealing with hypersonic flows, the implementation of chemical reactions is of fundamental importance. For the DSMC technique, a considerable number of chemistry models relevant for hypersonic aerothermodynamics have been developed [32, 39–45]. DSMC being a particle-based method, it is of fundamental importance to develop a molecular level chemistry model that predicts equilibrium and non-equilibrium reaction rates using only kinetic theory and fundamental molecular properties. In doing so, Bird [45] recently proposed a chemical reactions model based solely on the fundamental properties of the two colliding particles, i.e., total collision energy, the quantised vibrational levels, and the molecular dissociation energies. These models link chemical reactions and cross sections to the energy exchange process and the probability of transition between vibrational energy states. The Larsen-Borgnakke [46] procedures and the principle of microscopic reversibility are used to derive a simple model for recombination and reverse reactions. Called "Quantum-Kinetic", this DSMC chemistry model has been developed over the past years [45, 47–51] and it has been implemented and validated in the dsmcFoam code [52]. In the current implementation of the QK model in the dsmcFoam code, a 5-species air model with a total of 19 reactions is accounted for [52]. The QK chemistry model is used in this work to perform hypersonic flows simulations over the 3D cavities.

3. Computational parameters

In this section the computational parameters employed in the hypersonic flow simulations over 3D cavities are presented. These parameters are: the cavity geometry, freestream conditions, computational mesh and boundary conditions.

3.1. Geometry definition

In this work, panel-to-panel joints or TPS damage are modelled as three-dimensional cavities with a constant depth (D) and different lengths (L). By

considering that the cavity length is much smaller than the spacecraft characteristic length (R), i.e., $L/R \ll 1$, then the environmental conditions may be represented by hypersonic flow at zero angle of attack over a flat plate with a cavity positioned sufficiently far enough from the stagnation point.

Figure 3 shows a schematic of the 3D cavity and its main parameters. For the family of cavities investigated in this work, the cavity depth is fixed at 3 mm, while the length assumed values ranging from 3 to 15 mm. The upstream (L_u) and downstream (L_d) plates length and width (W_p) was kept constant with 50 mm and 4.5 mm, respectively. The cavity length-to-depth ratio (L/D) considered in this study was 1, 2, 3, 4, and 5.

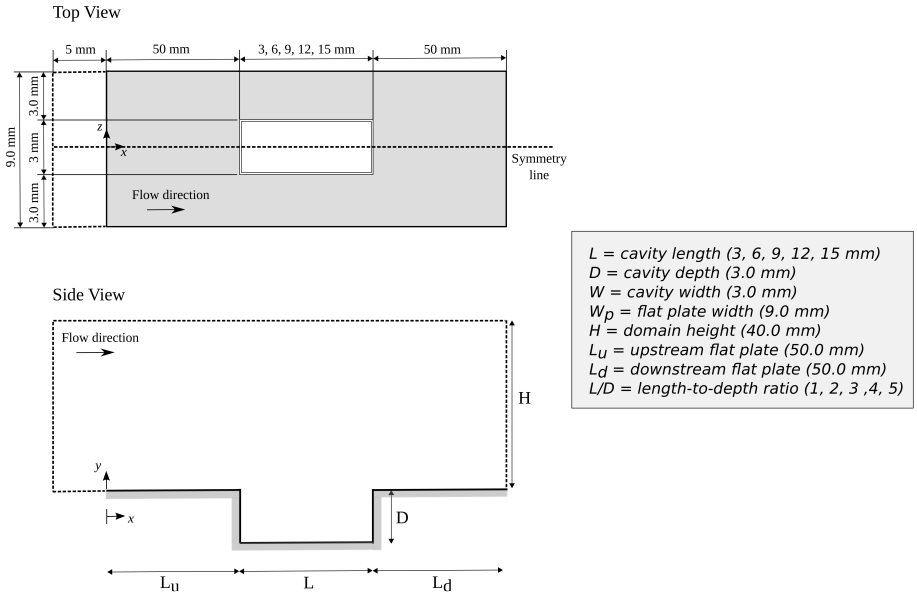

Figure 3: Schematic of the cavity configuration and its main geometrical parameters.

3.2. Freestream condition

The freestream conditions employed in the present calculations are shown in Table 1. The flow conditions represent those typically experienced by a reentry vehicle at an altitude of 80 km in the Earth's atmosphere and they can be found in the U.S. Standard Atmosphere tables [53]. At this altitude, the atmosphere

is composed of 78.8% nitrogen and 21.2% oxygen

Table 1: Freestream flow conditions at 80 km altitude.

Velocity (U_∞)	**Temperature** (T_∞)	**Pressure** (p_∞)	**Number density** (n_∞)	**Mean free path** (λ_∞)
7600 [m/s]	198.62 [K]	1.04 [Pa]	3.793×10^{20} [m^{-3}]	3.160×10^{-3} [m]

Assuming the cavity length L as the characteristic length, the global Knudsen numbers Kn_L are 1.053, 0.526, 0.351, 0.263, and 0.211 for cavity lengths of 3, 6, 9, 12, and 15 mm, respectively. The global Reynolds numbers Re_L are 31.45, 60.89, 91.34, 121.78, and 152.23 for cavity lengths of 3, 6, 9, 12, and 15 mm, respectively, based on the undisturbed freestream conditions. Therefore, the problem can be treated as laminar flow in the transitional regime.

3.3. Computational mesh and boundary conditions

In order to implement the DSMC procedure, the flowfield around the cavities is divided into a number of regions, which are subdivided into computational cells. The cells are smaller than the freestream mean free path and they are further subdivided into two subcells per cell in each coordinate direction. In the present work, the total number of cells employed varied from 1.05 to 1.28 million for L/D=1 and L/D=5, respectively. An example of computational mesh used in the present work are shown in Fig. 4. In particle simulations, time averaging of the flow properties is carried out in each cell after the establishment of steady state and a sufficient number of DSMC particles must be maintained in each computational cell, to compute the collisions adequately and to keep the statistical error under acceptable values [54, 55]. In previous verification and validation studies conducted with the dsmcFoam code [56] it was found that 15 to 20 particles per cell should be used in the high speed rarefied gas flows simulations to obtain accurate results.

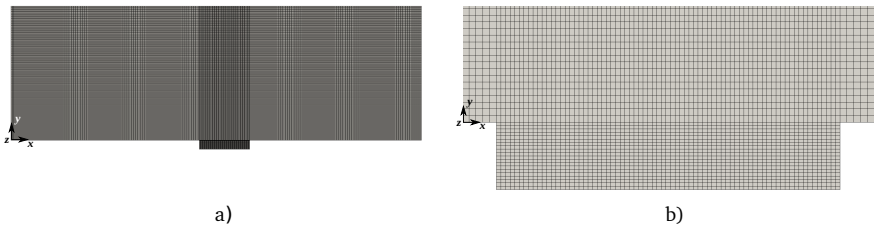

Figure 4: Computational mesh for L/D = 5 case: a) full domain, and b) mesh inside the cavity.

The computational domain used for the calculation is made large enough such that cavity disturbances do not reach the boundary condition at the top of the computational domain. At the inlets, the freestream conditions are specified and equal to those presented in Table 1. The inlet boundary conditions are imposed at 5 mm upstream of the L_u flat plate and the top inlet height (H) is defined at 40 mm above the cavity surface. At the outlet, vacuum was chosen as the boundary condition. Since the velocity at the exit is supersonic, the probability of a particle returning to the computational domain is very low [32].

The surface temperature T_w is assumed constant at 1000 K, which is chosen to be representative of the surface temperature near the stagnation point of a re-entry vehicle. It is important to highlight that the surface temperature is low compared to the stagnation temperature of the air. This assumption is reasonable since practical surface materials would be likely to disintegrate if the surface temperature approached the flow stagnation temperature. Diffuse reflection with complete momentum/thermal accommodation is applied at the wall boundary condition. The plane upstream of the L_u flat plate and at the centerline of the cavity are defined as symmetry planes, where all flow gradients normal to the these planes are zero. At the molecular level, this plane is equivalent to a specular reflecting boundary.

4. Computational results and discussion

In this section, the verification of the dsmcFoam code and the results obtained for reactive hypersonic gas flow over a family of cavities are presented. The main goal of this investigation is to characterise the influence of different L/D ratios on the macroscopic properties such as velocity, density, pressure, and temperature at rarefied conditions and compared with those characteristics found in the continuum regime. The macroscopic properties are measured for a series of vertical and horizontal profiles. Inside the cavities, the vertical profiles (P10 to P12) are taken at three different length positions, 0.25L, 0.50L, and 0.75L, respectively. Similarly, the horizontal profile measurements (P13 to P15) are located at three different cavity depths, 0.25D, 0.50D, and 0.75D, respectively.

4.1. Verification: Influence of computational parameters on the cavity surface quantities

In order to verify the dsmcFoam code used in the present investigation, it was considered the cavity length-to-depth ratio of 5. Simulations were performed with different mesh sizes, time steps, number of particles and number of samples. The effects of varying these quantities on the heat transfer (C_h), pressure (C_p) and skin friction (C_f) coefficient at the bottom cavity surface (S_3) was investigated.

The influence of the cell size on the aerodynamic surface quantities is shown in Figs. 5, at the left hand side. The standard structured mesh was created using a simple cuboid with $430 \times 134 \times 20$ cells in $x-$, $y-$, and $z-$ coordinate directions, respectively. The standard mesh is composed by 1.28 million of computational cells and each cell has a size of one third of the freestream mean free path. The standard for L/D = 5 is mesh is shown in Fig. 4. For the grid independence study, a coarse mesh was produced with half of computational cells employed in the standard mesh and the fine mesh was prepared with the double of cells used in the standard case. According to this group of plots, the

cell size demonstrated to be insensitive to the range of cell spacing considered indicating that the standard mesh is essentially grid independent.

A similar examination was conducted for the time step size. A reference time step of 3.78×10^{-9} s is chosen; this is significantly smaller than the freestream mean collision time and small enough to ensure particles will spend multiple time steps in a single cell. From Fig. 5, right hand side, it is noticed no alterations on the aerodynamic surfaces quantities when the time step is reduced or increased by a factor of four.

In addition to the mesh and time step sensitivity analysis, simulations were conducted in order to characterise the impact of the number of particles and samples on the computational results. Considering the standard mesh for L/D = 5 cases, with a total of 12.8 million particles, two new cases were investigated. Using the same mesh, it was employed 6.4 and 25.6 million particles in each simulation, respectively. In similar fashion, three different number of samples were considered in order to determine and minimise the statistical error. According to Fig. 6, a total of 12.8 million particles and 600,000 samples were necessary to fully solve the rarefied hypersonic flows over cavities.

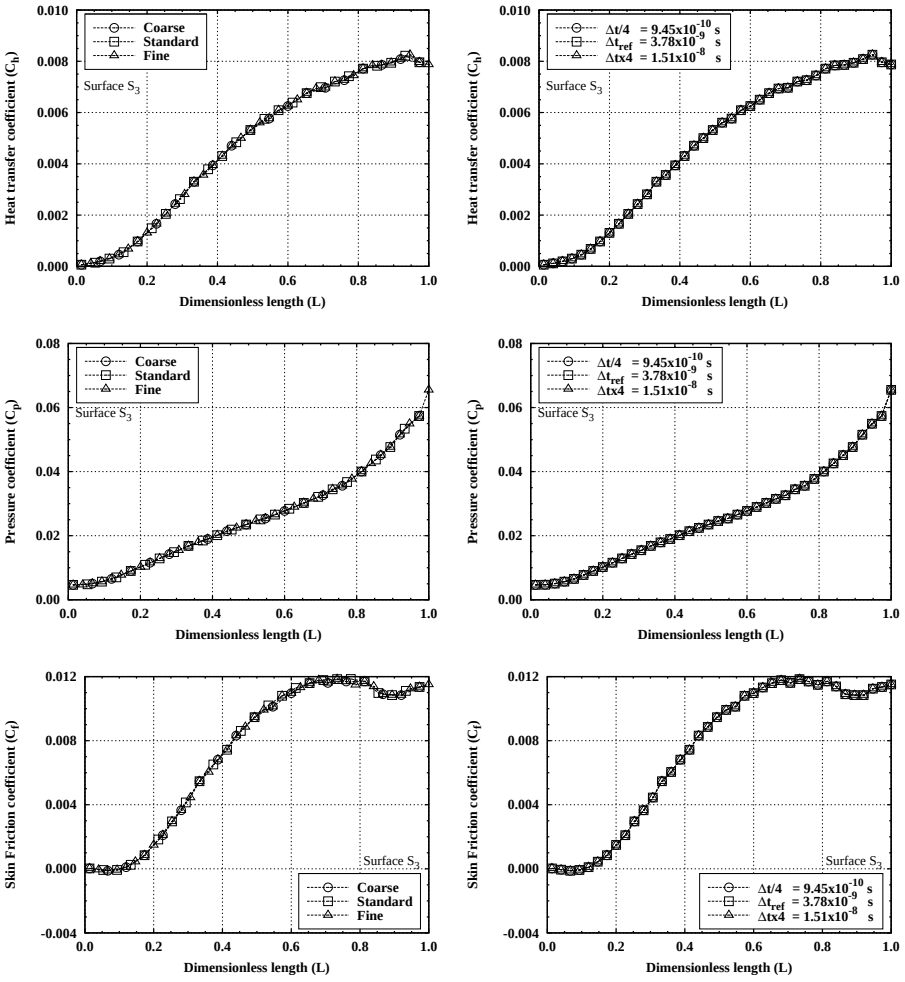

Figure 5: Influence of cell size and time step on aerodynamic surface quantities along the cavity bottom surface.

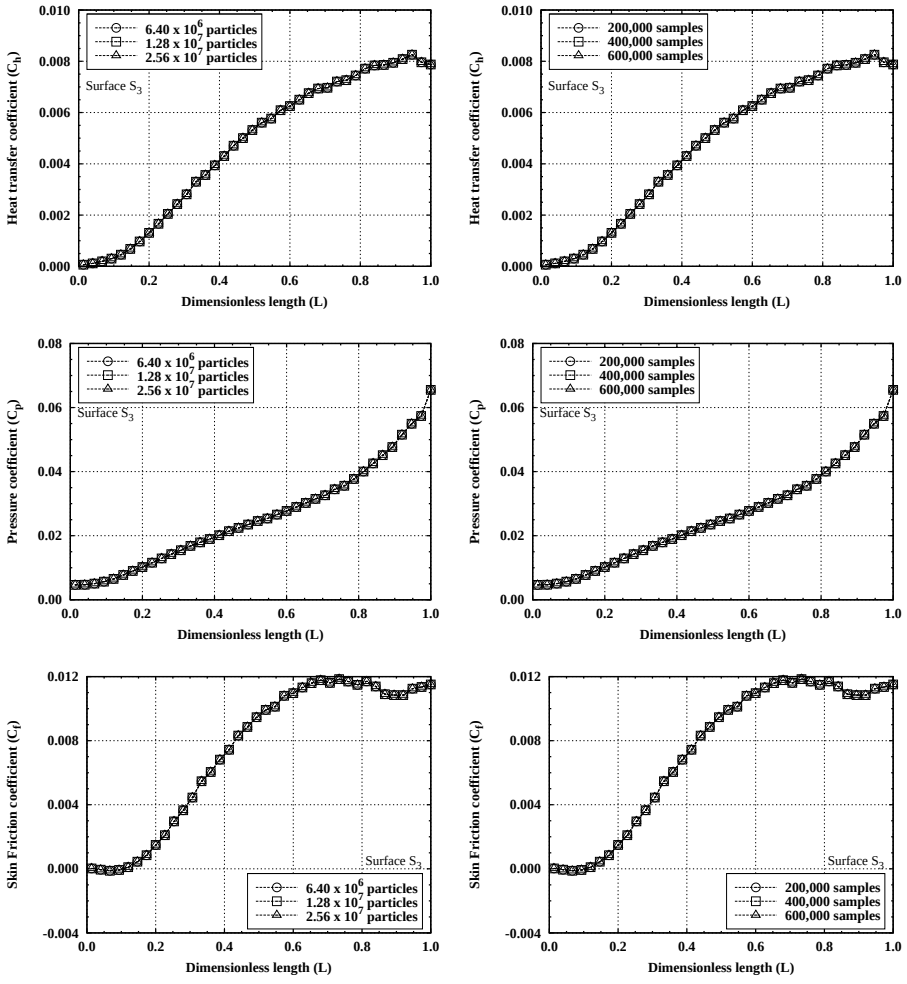

Figure 6: Influence of number of particles and number of samples on aerodynamic surface quantities along the cavity bottom surface.

4.2. The velocity flowfield

With the DSMC technique being a statistical method, the macroscopic properties are computed from local averages of the microscopic properties. Thus, the local macroscopic velocity vector is given by the following equation,

$$\mathbf{c}_0 = \frac{\overline{m\boldsymbol{c}}}{\overline{m}} = \frac{\sum_{j=1}^{N} m_j \boldsymbol{c}_j}{\sum_{j=1}^{N} m_j}, \tag{1}$$

where m and $\mathbf{c}$ represent the mass and the velocity vector of each individual particle, and N is the total number of simulated particles within a cell.

The impact of the cavity length-to-depth ratio on the velocity profiles inside the cavity is shown in Fig. 7. On examining Fig. 7 for the vertical velocity profiles on the left hand side, it is clear that the normalised velocity profiles are negative at the bottom of the cavities ($Y_D \approx$ -1). Moving upward, the velocity profiles becomes positive and reach a maximum value close to the cavities opening. At this location, it is interesting to notice that an increase in the length-to-depth ratio, from L/D = 1 to L/D = 5 leads to a velocity augmentation of 41% in the profile P10. In contrast, for the profile P12, the increment in the velocity was 21.2%. These results suggest that an expansion region and a compression zone have been formed around the upstream and downstream cavity lips, respectively. In order have a deeper understanding of the flowfield structure inside and around the cavities, the density, pressure, and temperature fields will be explored in the next sections.

Still referring to Fig. 7, it is clear that the velocity is reduced as the flow penetrates deeper into the cavity, from $Y_D = 0$ to $Y_D =$ -1. Furthermore, at location P15, close to the cavity bottom surface, a change in the flow topology inside the cavity is evident. For cavities of length-to-depth of 1 to 3, the velocity profiles are negative meaning that the flow is reversed along the cavity base. Nonetheless, for L/D = 5, the velocity achieves a minimum at location $X_L = 0.15$, increasing towards a positive value at $X_L = 0.275$ and reaching a maximum value at position $X_L = 0.55$. Also, the normalised velocity decreases

towards negative values at location $X_L = 0.92$ and increases again close to the downstream face of the cavity. For the cavity depth of L/D = 4, a similar trend is observed, however, the maximum positive velocity is not as prominent as in the L/D = 5 ratio case. These changes in the velocity signal are characteristic of the formation of more than one recirculation zone.

The velocity ratio (U/U_∞) contours with streamline traces over the computational inside the 3D cavities are shown in Fig. 8 for L/D ratios of 1, 2, 3, 4, and 5. It is evident that the flow inside cavities is characterised by recirculation structures. The streamline patterns for L/D ratios of 1 and 2 shows that the flow has a primary recirculation system which fills the entire cavity. A transition stage is evident for the case where the length-to-depth ratio is equal 3. In this case, the main flow is able to slightly penetrate and push the recirculation against the cavity bottom surface. In addition, due the force exerted by the mean flow in the recirculation, its shape is elongated and a secondary recirculation core is formed.

For the $L/D = 4$ and 5 cases, two vortices are formed, one of them close to the upstream face and the other in the vicinity of the downstream face of the cavity. The separated shear layer from the external stream does not reattach to the cavity floor, and the flow is reversed along the bottom cavity surface for the $L/D = 4$. However, for the $L/D = 5$ case the recirculation regions are well-defined and the separated shear layer is able to penetrate deeper into the cavity and attach to the cavity base wall, enhancing momentum and energy transfer to the bottom surface.

It is important to highlight that in the continuum regime, the two recirculation regions and flow attachment to the cavity bottom surface occurs when the length-to-depth ratio is equal to or greater than to 14. However, the same phenomena is observed in the transitional regime when the cavity L/D is equal to 5. In this case, even a small cavity under rarefied gas conditions could promote serious damage to the heat shield during reentry. The hot gases coming from the high temperature shock wave formed upstream of the vehicle may deeper penetrate the cavity and impinge directly in the bottom surface of the cavity.

This situation can lead to a premature degradation of the thermal protection system during the reentry phase.

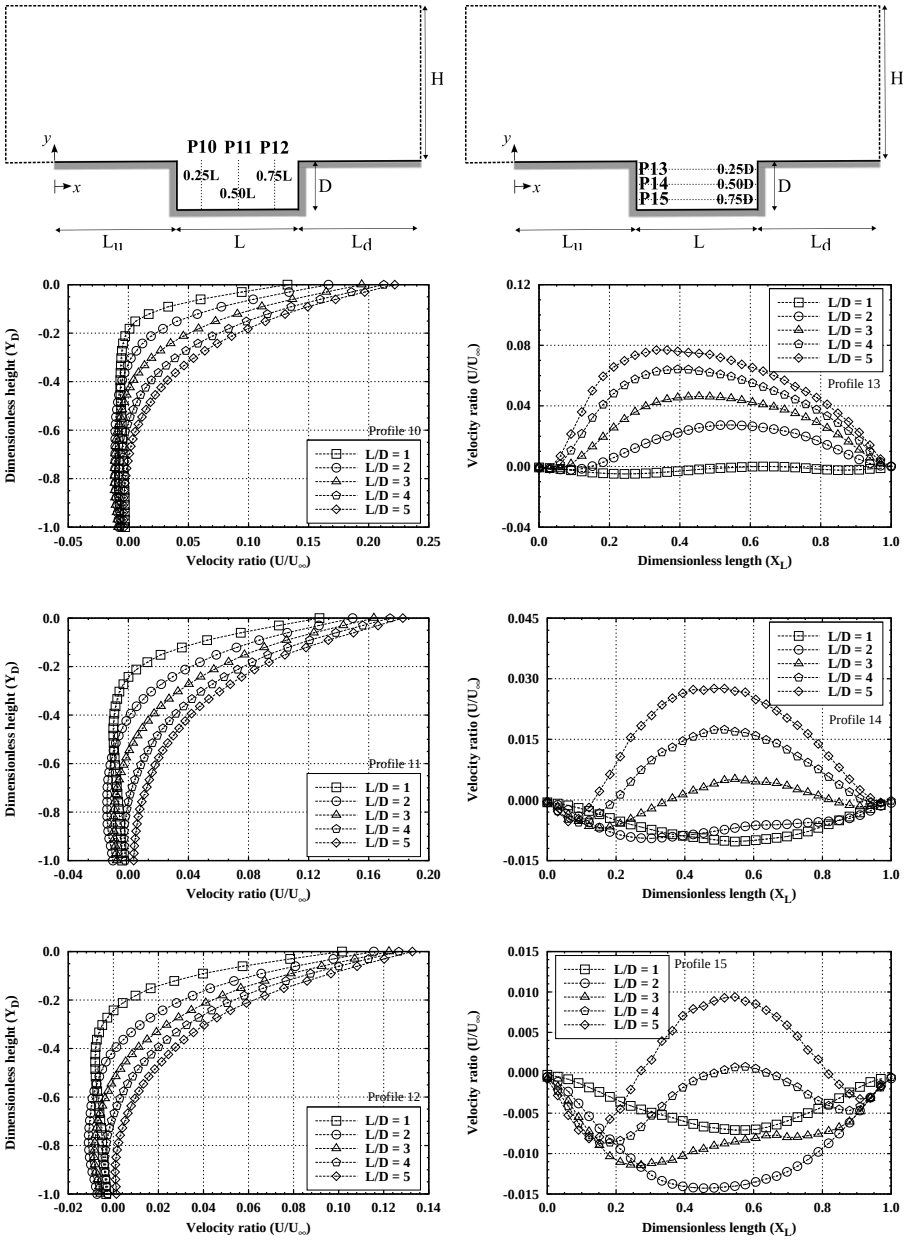

Figure 7: Velocity ratio (U/U_∞) profiles for six locations inside the cavity.

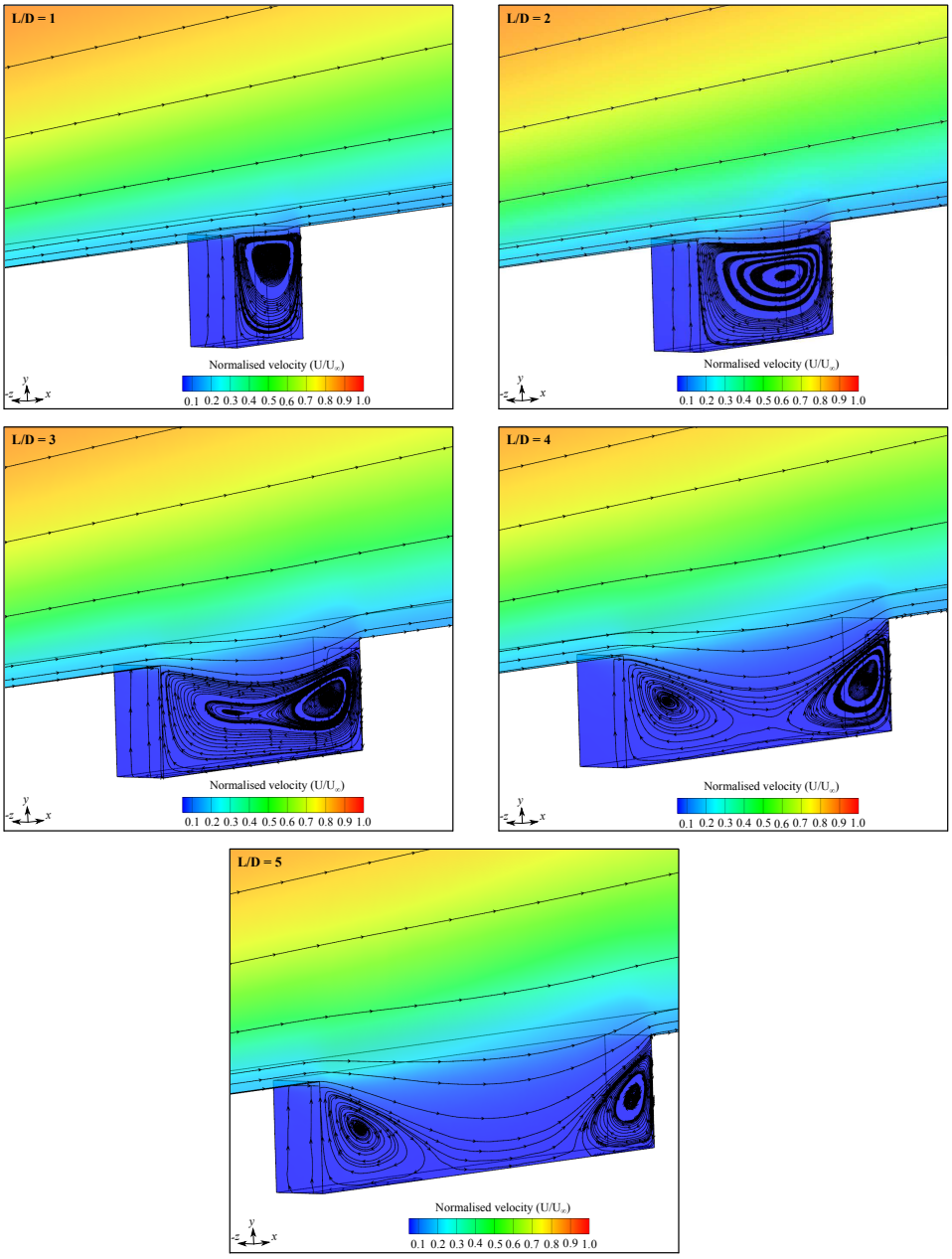

Figure 8: Velocity streamlines inside the cavities as a function of L/D ratio.

4.3. The density flowfield

The density within the computational cells on the *dsmcFoam* code is obtained using the following expression,

$$\rho = n\overline{m} = \frac{\overline{N}F_N}{V_c} = \frac{\sum_{j=1}^{N} m_j}{N}, \tag{2}$$

where n is the local number density, m is the molecular mass, and $\overline{N}$ and N are, respectively, the average and total number of simulated particles within a given cell. Furthermore, F_N represents the number of real atoms/molecules represented by a single DSMC particle, and V_c is the computational cell volume.

Figure 9 shows the normalised density profiles for six locations inside the cavity. From this group of plots, it is clear that the cavity length-to-depth ratio plays an important role in the density distribution inside the cavities. For profile 10 (P10), a slight decrease in the density up to location Y_D = -0.1 and an increase downwards to the cavity bottom surface is observed. Furthermore, it worth noticing that the density ratio is smaller than the freestream density ($\rho/\rho_\infty < 1$) for the cavities of L/D = 4 and 5. This is a important indication that an increased cavity length promotes a wake region close to the upstream vertical surface, with the characteristics of a flow expansion. In addition, L/D = 1 show the highest values of density ratio close to the bottom surface; however, at P12, the highest values are found for L/D = 4 and 5 due to the compression region at this location.

Three horizontal density profiles are shown on the right hand side of Fig. 9 as a function of the cavity length. According to these plots, the normalised density ratio for L/D = 3, 4, and 5 presented values below 1 up to position $X_L \approx 0.21$. This is evidence of flow expansion at this region. In the other hand, maximum values are found at X_L=1 where the particles are more likely to impinge directly on the cavity vertical face.

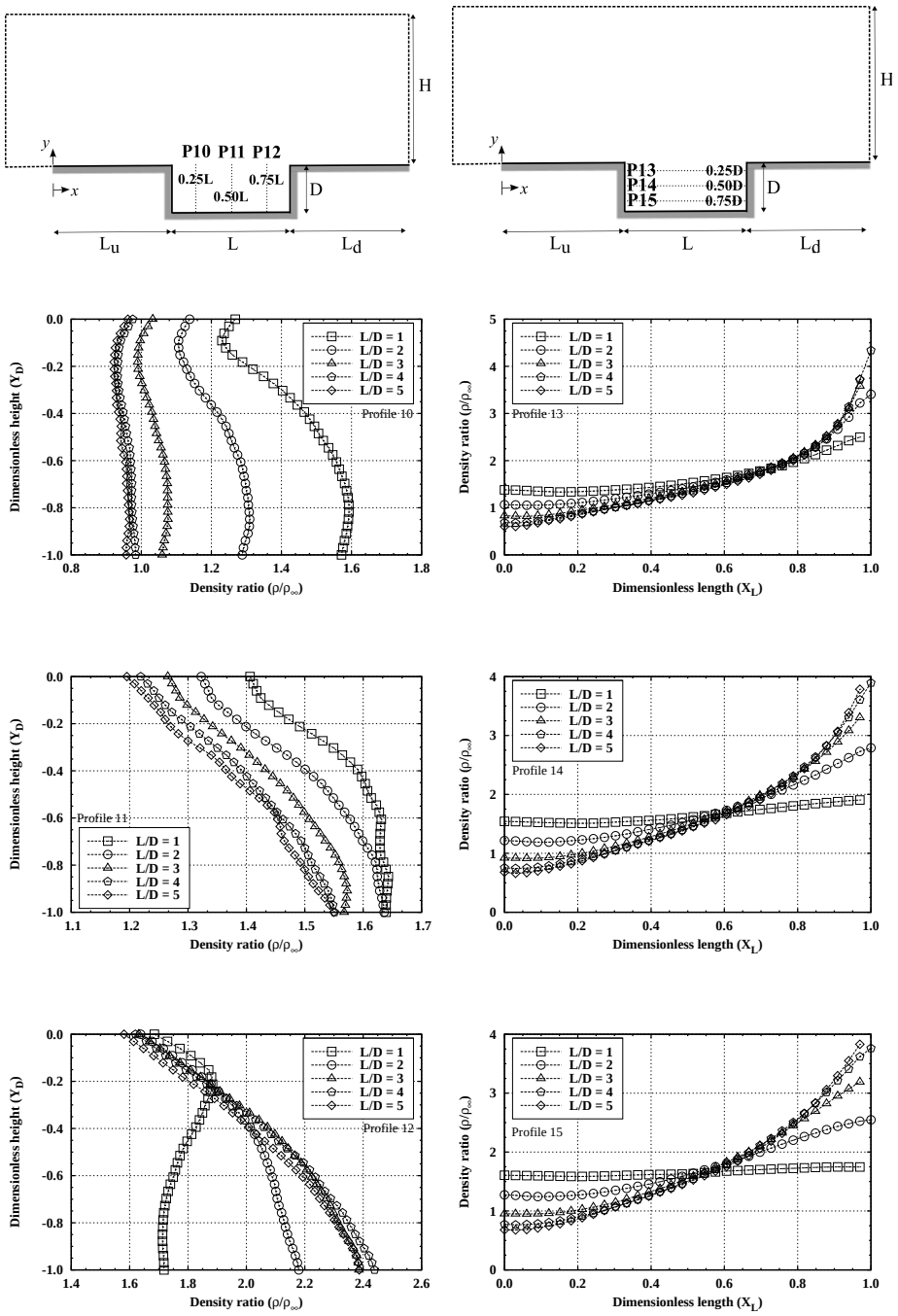

Figure 9: Density ratio (ρ/ρ_∞) profiles for six locations inside the cavity.

4.4. The pressure flowfield

The pressure determined by the *dsmcFoam* code is obtained using the following expression,

$$p = \frac{1}{3} n m \overline{\boldsymbol{c}'^2} = \frac{1}{3} \frac{\overline{N} F_N}{V_c} \frac{\sum_{j=1}^{N} m_j \boldsymbol{c}'^2}{N}, \tag{3}$$

where n is the local number density, m is the molecular mass, **c'** is the thermal velocity, $\overline{N}$ and N are, respectively, the average and total number of simulated particles within a given cell, and V_c is the computational cell volume.

The effects of the L/D ratio on the pressure profiles located inside the cavities are shown in Fig. 10. In this set of plots, the left and right columns correspond to the horizontal and vertical profiles, respectively. Firstly, on the left hand side, it is evident that the pressure ratio inside the cavities decreases from the top to the bottom of the cavities for the range of L/D ratio investigated. Furthermore, the pressure ratio at P12 at the bottom of the cavity for L/D = 5 is twice larger that one found for L/D = 1.

Analysing Fig. 10, on the right hand side, it is observed that the pressure is low at $X_L = 0$, increases as flow flow moves inside the cavities, and reaches a maximum value at $X_L = 1$. It is worth to notice that the pressure ratio for L/D = 5 at $X_L = 1$ is 50 times higher than in $X_L = 0$ at P13. However, this difference in the pressure ratio decrease 30 times in the cavity bottom surface, at profile 15.

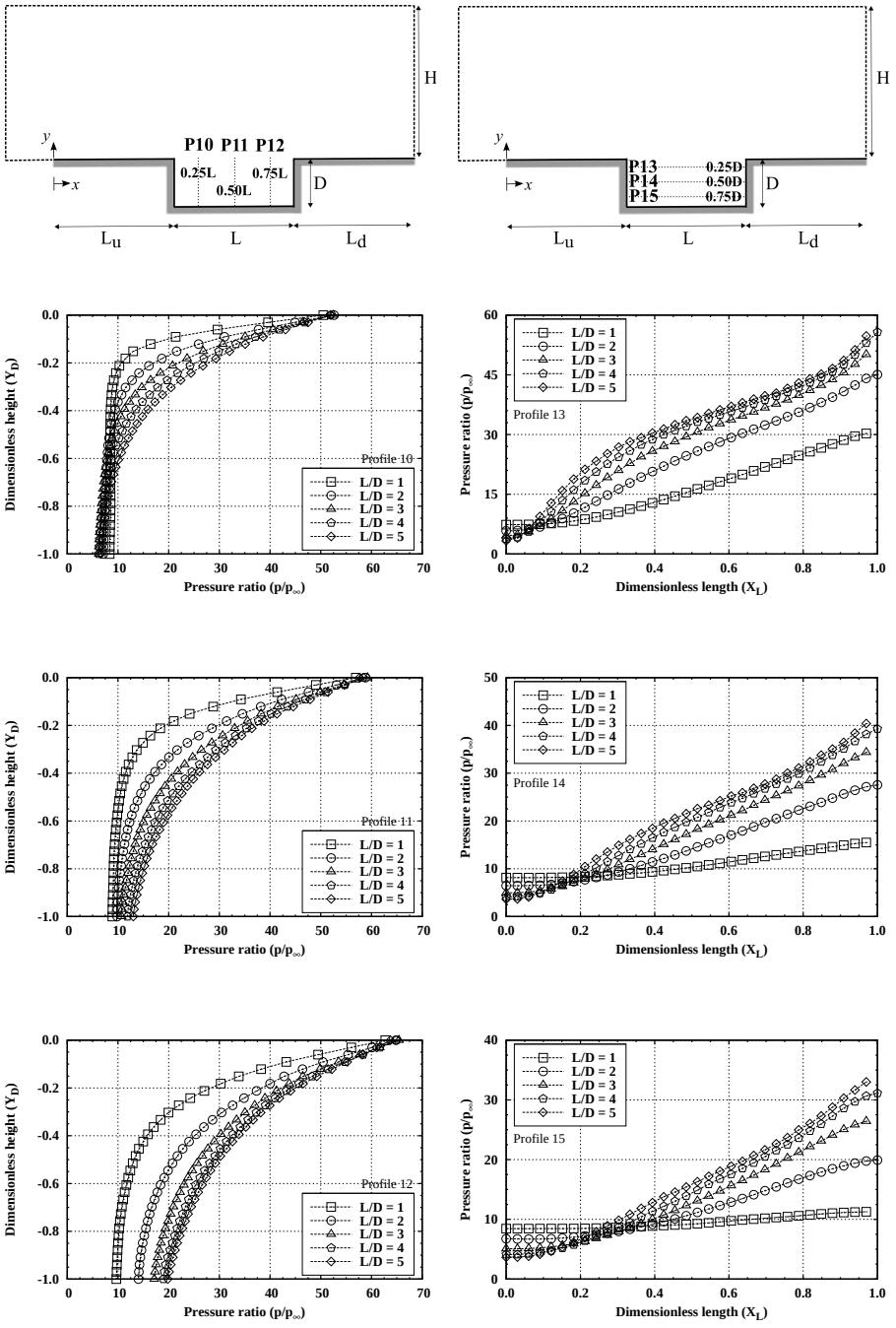

Figure 10: Pressure ratio (p/p_∞) profiles for six locations inside the cavity.

4.5. The temperature flowfield

During atmospheric reentry, bow shock formation is one of the main characteristics of hypersonic flight. Across the shock wave, part of the high kinetic energy present in the flow is rapidly converted to thermal energy, significantly increasing on the temperature and pressure in the shock region. As a consequence of the temperature augmentation, the molecules which surround the re-entry vehicle become highly excited and chemical reactions are likely to occur as thermal-kinetic energy exchange are performed by successive intermolecular interactions. Following this, a relaxation process between translational and internal modes takes place leading each mode towards the equilibrium state. Thermodynamic equilibrium occurs when there is, statistically, complete energy equipartition between translational and internal modes. In this sense, the thermodynamic temperature is defined when the temperatures based on each energy mode, i.e., translational, rotational, vibrational, and electronic temperatures, are equal to each other. However, the relaxation time, commonly expressed in terms of the relaxation collision number, differs from one mode to another. Therefore, thermal nonequilibrium arises if the local collision frequency is not sufficient to return the molecules to the total statistical equilibrium. In this scenario, for a gas in chemical and thermodynamic nonequilibrium, the overall temperature (T_{ov}) is defined as the weighted average of the translational (T_{tra}), rotational (T_{rot}), and vibrational (T_{vib}) with respect to the degrees of freedom ($\overline{\zeta}$) of each mode [32], as follow:

$$T_{ov} = \frac{3T_{tra} + \overline{\zeta}_{rot}T_{rot} + \overline{\zeta}_{vib}T_{vib}}{3 + \overline{\zeta}_{rot} + \overline{\zeta}_{vib}}. \tag{4}$$

Translational, rotational and vibrational temperatures are obtained for each cell in the computational domain through the following equations,

$$T_{tra} = \frac{1}{3k_B}\overline{m\boldsymbol{c}'^2} = \frac{1}{3k_B}\frac{\sum_{j=1}^{N} m_j \boldsymbol{c}'^2}{N}, \tag{5}$$

$$T_{rot} = \frac{2m\varepsilon_{rot}}{k_B\zeta_{rot}} = \frac{2}{k_B\zeta_{rot}} \frac{\sum_{j=1}^{N}(\varepsilon_{rot})_j}{N}, \tag{6}$$

$$T_{vib} = \frac{\Theta_{vib}}{ln\left(1 + \frac{k_B\Theta_{vib}}{\overline{\varepsilon}_{vib}}\right)} = \frac{\Theta_{vib}}{ln\left(1 + \frac{k_B\Theta_{vib}}{\sum_{j=1}^{N}(\varepsilon_{vib})_j}\right)}. \tag{7}$$

where k_B represents the Boltzmann constant, $\overline{\varepsilon}_{rot}$ and $\overline{\varepsilon}_{vib}$ are average rotational and vibrational energies per particle computed within the respective cell, and Θ_{vib} the characteristic vibrational temperature.

In a different manner from the previous sections, the temperature profiles are presented here for cavity length-to-depth ratios equal to 1 and 5, i.e, 3 mm and 15 mm length, respectively. From L/D = 2 to 4, the results are intermediate and will not be presented.

Figure 11 presents the temperature ratio profiles inside the cavities. The vertical and horizontal temperature profiles are shown as a function of the cavity depth and length, respectively.

According to Fig. 11, on the left hand side, a high temperature ratio is observed at the top of the cavity, due the shock wave expansion ant the leading edge of L_u flat plate. Moving towards the cavity bottom surface, the temperatures decrease and reach minimum values at the bottom surface. In addition, it is worth highlighting a high degree of thermodynamic nonequilibrium at the cavity opening, however, as the flow moves downwards, the conditions are driven towards thermodynamics equilibrium. At the bottom surface, the temperature highest value is found for the L/D = 5 and do no exceed 8.3 times the freestream temperature.

It is important to remark that the translational temperature at the top of the cavity for L/D = 5 at location P10 is 23.8% higher than P12. As P10 is characterised by a expansion region, a temperature decrease was anticipated in this region; however, the increase observed at P10 is associated with the high temperature generated by the attached shock wave on the upstream plate (L_u).

Figure 11, on the right hand side, presents the temperature ratio for 3 horizontal profiles inside the cavities. From this group of plots it is clear that when the cavity length-to-depth ratio is increased, there is a significant change on temperature inside the cavity. For L/D = 1 and 5, the temperatures values up to location $X_L = 0.1$ are similar and reach the value of $5T_\infty$. From $X_L = 0.1$ to $X_L = 0.8$, the translational temperature for the L/D = 5 case at P15 is 7.5 times higher to those observed for L/D = 1. However, at profile P13 located close to the cavity opening, the temperature for L/D = 5 is 13.3 times higher when compared with L/D = 1. In addition, it is noticed that the translational temperature ratio for L/D = 5 is decreased from $25.3T_\infty$ at P13, cavity opening, to $12.5T_\infty$ at P15, cavity bottom surface. Furthermore, as the temperature ratio for L/D = 5 is 12.5 times higher than the freestream temperature (198.62 K), such a temperature is greatly in excess of the melting point of the airframe structure and could lead a catastrophic reentry and loss of the vehicle.

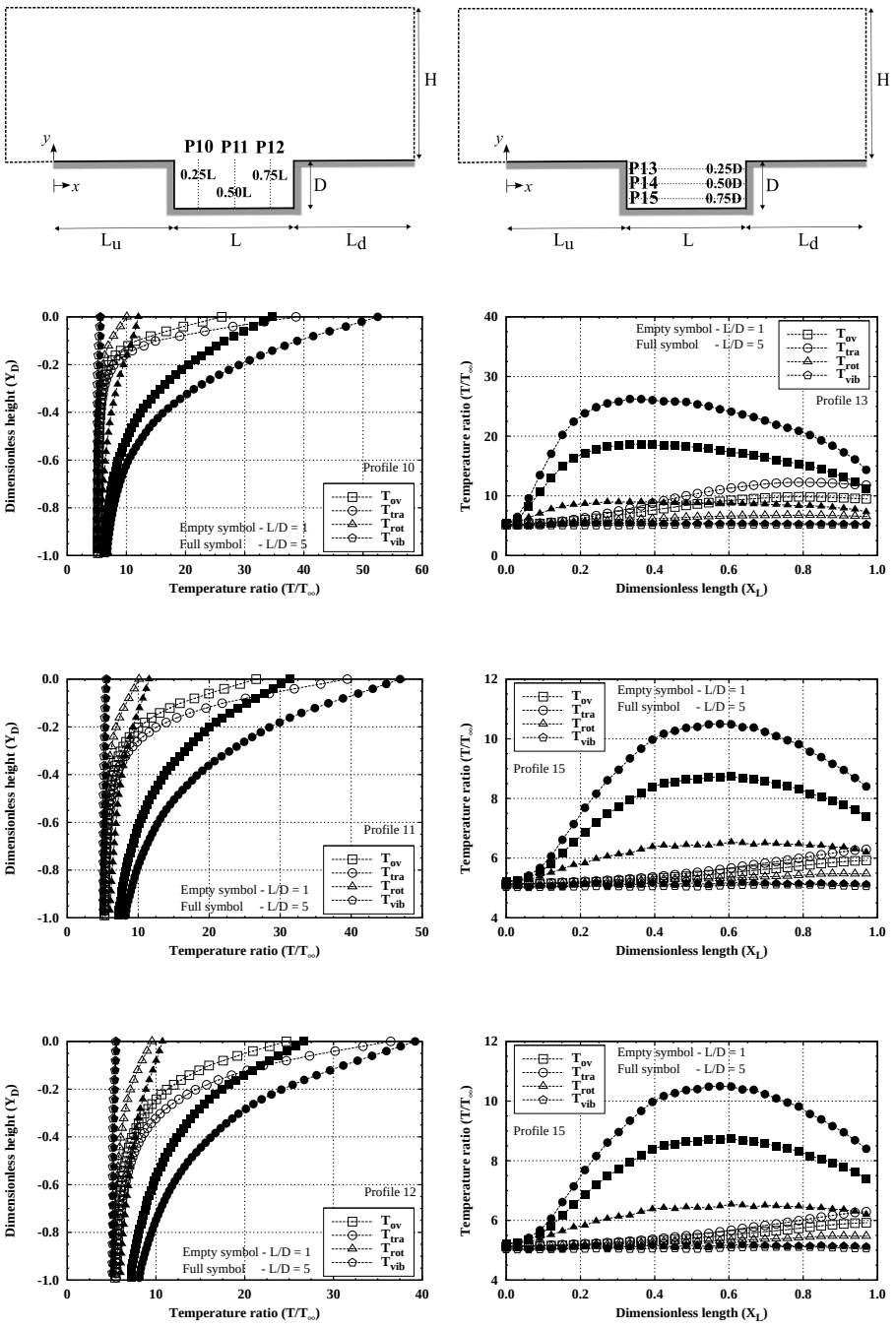

Figure 11: Temperature ratio (T/T_∞) profiles for six locations inside the cavity.

5. Conclusions

In this paper, rarefied hypersonic gas flows simulations over three-dimensional cavities, representative of panel-to-panel joints, have been performed by using the DSMC method. The main focus of this computational work was to investigate and characterise the influence of the L/D ratio on the flowfield structure around and inside the cavities under rarefied conditions. In this investigation, the cavity depth was kept constant at 3 mm and the cavity length assumed different values ranging from 3 to 15 mm (L/D = 1, 2, 3, 4, and 5). The freestream conditions used corresponded to that experienced by a re-entry vehicle at a velocity of 7600 m/s and an altitude of 80 km. At this condition, chemical reactions are likely to occur and the Quantum-Kinetic chemistry model was employed to simulate a 5-species air model with a total of 19 reactions.

In order to characterise the flowfield structure, the macroscopic properties were measured at different positions inside the cavities. According to the computed results for cavity L/D ratios of 1 and 2, it is observed that an increase in particle density inside the cavities occurs, demonstrating that most particles remain in the cavities. Consequently, the high concentration of particles inside these cavities do not allow the penetration of the incoming freestream to take place. The main characteristics of these cavities is the presence of a single recirculation zone which fills the entire the cavity. When the L/D ratio is increased to 3, it is evident that there is a tendency to form a new recirculation region due the appearance of another rotating zone. At this L/D ratio, the recirculation is more elongated when compared with the previous two cases. More importantly, it is observed that a significant increase in the density, pressure, and temperature occurs in the region close to right hand side cavity vertical wall as a result of flow penetration and the direct impact of particles against this wall. The increase of these macroscopic properties at this region indicates that the flow is able to partially penetrate the cavity, which in turn, leads to the formation a shock structure at the junction between the vertical plate and the downstream flat plate (L_d). According to the continuum regime, this phenomena occurs for

cavity length-to-depth ratios between 10 and 14.

Analysing the results for L/D ratios of 4 and 5, the formation of two recirculation regions inside the cavities is observed. The formation of these recirculation regions are even more clear when the velocity profile P_{15} is considered. In this profile the recirculation region is detected when velocity profile changes from positive to negative close to left vertical plate and negative to positive in the right vertical cavity plate. In these two cases, the main flow is able to penetrate even into deeper the cavities, however, only in the case where L/D is equal to 5 the flow impinges directly onto the bottom surface. Examining the distribution of density, pressure, and temperature along the profile P_{15}, it is noticed that the macroscopic properties are several times larger than those computed for a cavity L/D = 1. This constitutes a potentially dangerous situation for a reentry vehicle since the hot gas from the shock wave formed upstream of the vehicle may enter the cavity and raise the temperature of the aluminium structure above its melting point. Moreover, twin recirculation zones and flow penetration appear to only occur in the continuum regime for length-to-depth ratios greater than 14.

Comparing the results obtained in the transitional regime using the DSMC method with those available in the literature for the continuum regime, rarefied gas flows over 3D cavities can be classified as follow: i) open cavity for L/D = 1 and 2; ii) transitional cavity for L/D = 3; and iii) closed cavity for L/D = 3 and 4. For the conditions investigated, the main features of each cavity are summarised in Figure 12.

6. Acknowledgements

The authors gratefully acknowledge the partial support for this research provided by Conselho Nacional de Desenvolvimento Científico e Tecnológico, CNPq, under the Research Grant No.200473/2010-7. The authors are also indebted to the partial financial support received from Fundação de Amparo à Pesquisa do Estado de São Paulo, FAPESP, under the Research Grant No. 2014/25438-1.

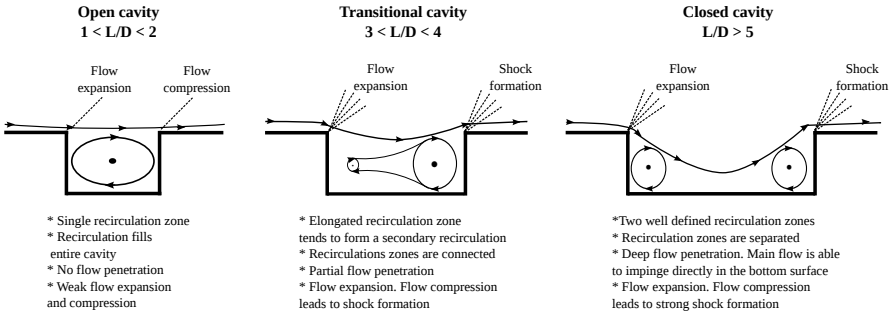

Figure 12: Rarefied reactive hypersonic gas flows over cavities in the transitional regime.

The reactive rarefied gas flows simulations over the 3D cavities were performed using the dsmcFoam code developed by the James Weir Fluids Laboratory based at the University of Strathclyde, Glasgow-UK.

References

[1] G. W. Sutton, The temperature history in a thick skin subjected to laminar heating during entry into the atmosphere, Journal of Jet Propulsion 28 (1) (1958) 40–45.

[2] G. W. Sutton, The initial development of ablation heat protection, an historical perspective, Journal of Spacecraft and Rockets 19 (1) (1982) 3–11.

[3] D. R. Tenney, W. B. Lisagor, S. C. Dixon, Materials and structures for hypersonic vehicles, Journal of Aircraft 26 (11) (1989) 953–970.

[4] J. C. Dunavant, D. A. Throckmorton, Aerodynamic heat transfer to RSI tile surfaces and gap intersections, Journal of Spacecraft and Rockets 6 (6) (1974) 437–440.

[5] C. A. Belk, J. H. Robinson, M. B. Alexander, W. J. Cooke, Pavelitz, Meteoroids and orbital debris: effects on spacecraft, Tech. Rep. NASA-1408 (1997).

[6] S. Evans, J. Williamsen, Orbital debris shape and orientation effects on impact damage to shuttle tiles, in: 47th Structures, Structural Dynamics, and Materials Conference, no. AIAA Paper 2006-2221, Newport, RI, 2006.

[7] G. E. Palmer, C. Tang, Computational assessment of the thermal protection system damage experienced during STS-118, Journal of Spacecraft and Rockets 46 (6) (2009) 1110–1116.

[8] J. L. Everhart, F. A. Greene, Turbulent supersonic/hypersonic heating correlations for open and closed cavities, Journal of Spacecraft and Rockets 47 (4) (2010) 545–553.

[9] C. H. Campbell, R. A. King, S. A. Berry, M. A. Kegerise, T. J. Horvath, Roles of engineering correlations in hypersonic entry boundary layer transition prediction, in: 48th AIAA Aerospace Sciences Meeting Including the New Horizons Forum and Aerospace Exposition, Orlando, Florida, 2010.

[10] M. H. Bertran, M. M. Wiggs, Effect of surface distortions on the heat transfer to a wing at hypersonic speeds, AIAA Journal 1 (6) (1963) 1313–1319.

[11] D. E. Nestler, A. R. Saydah, W. L. Auxer, Heat transfer to steps and cavities in hypersonic turbulent flow, AIAA Journal 7 (7) (1968) 1368–1370.

[12] J. W. Hodgson, Heat transfer in separated laminar hypersonic flow, AIAA Journal 8 (12) (1970) 2291–2293.

[13] R. A. Brewer, A. R. Saydah, D. E. Nestler, D. E. Florence, Thermal performance evaluation of RSI panel gaps for space shuttle orbiter, Journal of Spacecraft and Rockets 10 (1) (1973) 23–28.

[14] I. Weintein, D. E. Avery, A. J. Chapman, Aerodynamic heating to the gaps and surfaces of simulated reusable-surface-insulation tile array in turbulent flow at Mach 6.6, Tech. Rep. NASA TM-3225 (1975).

[15] A. R. Wieting, Experimental investigation of heat-transfer distributions in deep cavities in hypersonic separated flow, Tech. Rep. NASA TN-5908 (1970).

[16] H. L. Bohon, J. Sawyer, L. R. Hunt, I. Weintein, Performance of thermal protection systems in a Mach 7 environment, Journal of Spacecraft and Rockets 12 (12) (1975) 744–749.

[17] J. J. Bertin, Aerodynamic heating for gaps in laminar and transitional boundary layers, in: 18th Aerospace Science Meeting, Pasadena, California, 1980.

[18] D. P. Rizzetta, Numerical simulation of supersonic flow over a three-dimensional cavity, AIAA Journal 26 (7) (1988) 799–807.

[19] F. L. J. Wilcox, Experimental measurements of internal store separation characteristics at supersonic speeds, in: Royal Aeronautical Society Conference, Bath, United Kingdom, 1990, pp. 5.1–5.16.

[20] R. L. J. Stallings, D. K. Forrest, Separation characteristics of internally carried stores at supersonic speeds, Tech. Rep. NASA TP-2993 (1990).

[21] X. Zhang, E. Morishita, H. Itoh, Experimental and computational investigation of supersonic cavity flows, in: 10th AIAA/NAL-NASDA-ISAS International Space Planes and Hypersonic Systems and Technologies Conference, no. AIAA Paper 2001-1755, Hyoto, Japan, 2001.

[22] A. P. Jackson, R. Hiller, S. Soltani, Experimental and computational study of laminar cavity flows at hypersonic speeds, Journal of Fluid Mechanics 427 (2001) 329–358.

[23] M. A. Pulsonetti, W. A. Wood, Computational aerothermodynamic assessment of space shuttle orbiter tile damage - open cavities, in: 38th AIAA Thermophysics Conference, Toronto, Canada, 2005.

[24] J. L. Everhart, S. J. Alter, N. R. Merski, W. A. Wood, R. K. Prabhu, Pressure gradient effects on hypersonic cavity flow heating, in: 44th AIAA Aerospace Sciences Meeting and Exhibit, Reno, Nevada, 2006.

[25] J. L. Everhart, K. T. Berger, K. S. Bey, N. R. Merski, W. A. Wood, Cavity heating experiments supporting shuttle Columbia accident investigation, Tech. Rep. NASA TN-2011-214528 (2011).

[26] A. Mohammadzadeh, E. Roohi, H. Niazmand, S. Stefanov, R. S. Myong, Thermal and second-law analysis of a micro-or nanocavity using direct simulation Monte Carlo, Physical Review E 85 (5) (2012) 0563101–05631011.

[27] C. D. Robinson, J. K. Harvey, A parallel dsmc implementation on unstructured meshes with adaptive domain decomposition, in: Proceedings of the 20th International Symposium on Rarefied Gas Dynamics, Beijing , China, 1996.

[28] R. C. Palharini, T. J. Scanlon, J. M. Reese, Aerothermodynamic comparison of two-and three-dimensional rarefied hypersonic cavity flows, Journal of Spacecraft and Rockets 51 (5) (2014) 1619–1630.

[29] B. John, X. Gu, D. R. Emerson, Effects of incomplete surface accommodation on non-equilibrium heat ttransfer in cavity flow: A parallel DSMC study, Computers & Fluids 45 (1) (2011) 197–201.

[30] C.A.I.-Board, Report of the space shuttle columbia accident investigation, Tech. rep., National Aeronautics and Space Administration, Washington, D.C (August 2003).

[31] C. H. Campbell, B. Anderson, G. Bourland, S. Bouslog, A. Cassady, T. J. Horvath, S. A. Berry, P. A. Gnoffo, W. A. Wood, J. J. Reuther, D. M. Driver, D. C. Chao, J. Hyatt, Orbiter return to flight entry aeroheating, in: 9th AIAA/ASME Joint Thermophysics and Heat Transfer Conference, no. AIAA Paper 2006-2917, San Francisco, California, 2006.

[32] G. Bird, Molecular Gas Dynamics and the Direct Simulation of Gas Flows, Clarendon, Oxford, 1994.

[33] C. Cercignani, Rarefied gas dynamics: from basic concepts to actual calculations, Cambridge University Press, 2000.

[34] E. Roohi, S. Stefanov, Collision partner selection schemes in DSMC: From micro/nano flows to hypersonic flows, Physics Reports 656 (2016) 1–38.

[35] F. J. Alexander, A. L. Garcia, B. J. Alder, Cell size dependence of transport coefficients in stochastic particle algorithms, Physics of Fluids 10 (6) (1998) 1540–1542.

[36] F. J. Alexander, A. L. Garcia, B. J. Alder, Erratum: Cell size dependence of transport coefficients in stochastic particle algorithms [Phys. Fluids 10, 1540 (1998)], Physics of Fluids 12 (3) (2000) 731.

[37] A. G. Garcia, W. A. Wagner, Time step truncation error in direct simulation Monte Carlo, Physics of Fluids 12 (10) (2000) 2621–2633.

[38] N. G. Hadjiconstantinou, Analysis of discretization in the direct simulation Monte Carlo, Physics of Fluids 12 (10) (2000) 2634–2638.

[39] C. Rebick, R. D. Levine, Collision induced dissociation: A statistical theory, Journal of Chemical Physics 58 (9) (1973) 3942–3952.

[40] K. A. Koura, A set of model cross sections for the Monte Carlo simulation of rarefied real gases: atom-diatom collisions, Physics of Fluids 6 (1994) 3473–3486.

[41] I. D. Boyd, A threshold line dissociation model for the direct simulation Monte Carlo method, Physics of Fluids 8 (1996) 1293–1300.

[42] M. A. Gallis, Maximum entropy analysis of chemical reaction energy dependence, Journal of Thermophysics and Heat Transfer 10 (1996) 217–223.

[43] G. A. Bird, Simulation of multi-dimensional and chemically reacting flows (past space shuttle orbiter), in: 11th International Symposium on Rarefied Gas Dynamics, 1979, pp. 365–388.

[44] I. D. Boyd, Assessment of chemical nonequilibrium in rarefied hypersonic flow, in: 28th Aerospace Sciences Meeting, no. AIAA Paper 90-0145, 1990.

[45] G. A. Bird, The QK model for gas-phase chemical reaction rates, Physics of Fluids 23 (10) (2011) 106101.

[46] C. Borgnakke, P. S. Larsen, Statistical collision model for Monte Carlo simulation of polyatomic gas mixture, Journal of Computational Physics 18 (4) (1975) 405–420.

[47] G. A. Bird, A comparison of collision energy-based and temperature-based procedures in DSMC, in: 26th International Symposium on Rarified Gas Dynamics, Vol. 1084, Kyoto, Japan, 2008, pp. 245–250.

[48] M. A. Gallis, R. B. Bond, J. Torczynski, A kinetic-theory approach for computing chemical-reaction rates in upper-atmosphere hypersonic flows, Journal of Chemical Physics 138 (124311).

[49] G. A. Bird, Chemical reactions in DSMC, in: 27th Symposium on Rarefied Gas Dynamics, Pacific Grove, CA, 2010.

[50] G. A. Bird, The quantum-kinetic chemistry model, in: 27th International Symposium on Rarefied Gas Dynamics, Pacific Grove, CA, 2010.

[51] I. Wysong, S. Gimelshein, N. Gimelshein, W. McKeon, F. Esposito, Reaction cross sections for two direct simulation Monte Carlo models: Accuracy and sensitivity analysis, Physics of Fluids 24 (042002).

[52] T. J. Scanlon, C. White, M. K. Borg, R. C. Palharini, E. Farbar, I. D. Boyd, J. M. Reese, R. E. Brown, Open-source direct simulation Monte Carlo chemistry modeling for hypersonic flows, AIAA Journal 53 (6) (2015) 1670–1680.

[53] U. S. Atmosphere, National oceanic and atmospheric administration, Aeronautics and Space Administration, United States Air Force, Washington, DC.

[54] M. Fallavollita, D. Baganoff, J. McDonald, Reduction of simulation cost and error for particle simulations of rarefied flows, Journal of Computational Physics 109 (1) (1993) 30–36.

[55] G. Chen, I. D. Boyd, Statistical error analysis for the direct simulation Monte Carlo technique, Journal of Computational Physics 126 (2) (1996) 434–448.

[56] R. C. Palharini, C. White, T. J. Scanlon, R. E. Brown, M. K. Borg, J. M. Reese, Benchmark numerical simulations of rarefied non-reacting gas flows using an open-source DSMC code, Computers & Fluids 120 (2015) 140–157.